Three-Dimensional Quantitative Flow Visualization Around a Thrust Reverser

Hysa, Ilda; Tuinstra, Marthijn; Sciacchitano, Andrea; Scarano, Fulvio; Schwartz, Nicholas; Harrison, Charles; Gebbink, Roy

DOI
10.2514/1.J063124

Publication date
2023

Document Version
Final published version

Published in
AIAA Journal

Citation (APA)
Hysa, I., Tuinstra, M., Sciacchitano, A., Scarano, F., Schwartz, N., Harrison, C., & Gebbink, R. (2023). Three-Dimensional Quantitative Flow Visualization Around a Thrust Reverser. *AIAA Journal*, *61*(12), 5404-5414. https://doi.org/10.2514/1.J063124

AIAA JOURNAL
Vol. 61, No. 12, December 2023

Three-Dimensional Quantitative Flow Visualization Around a Thrust Reverser

Ilda Hysa* and Marthijn Tuinstra†
Netherlands Aerospace Centre/NLR, 8316 PR Marknesse, The Netherlands
Andrea Sciacchitano‡ and Fulvio Scarano§
Delft University of Technology, 2629 HS Delft, The Netherlands
Nicholas Schwartz¶ and Charles Harrison**
Gulfstream Aerospace Corporation, Savannah, Georgia 31408
and
Roy Gebbink††
German–Dutch Wind Tunnels, 8316 PR Marknesse, The Netherlands

https://doi.org/10.2514/1.J063124

Volumetric particle tracking velocimetry measurements are performed in a low-speed wind tunnel to study the flow around a 1:12-scale aircraft model with jet engines operating with thrust reversers. The engine jet and freestream flow velocity are varied to yield a jet to freestream velocity ratio of V_{jet}/V_{∞} ranging from 1.5 to 6. Measurements at such scale (0.5 m^3) require the use of strongly scattering helium-filled soap bubbles as flow tracers, which are introduced in both the jet and the freestream flow. The tracer's three-dimensional motion is determined using an array of cameras and a Lagrangian particle tracking algorithm. The mean velocity field reveals the jet inner structure as well as its interaction with the freestream, the ground board, the nacelle, the fuselage, and the horizontal and vertical tails. The experiments allow detection of exhaust reingestion as well as the aerodynamic interference with control surfaces at the tail segments in a single measurement volume. The results are in good agreement with conventional temperature rake measurements while adding details of the flow topology and of the large-scale unsteady flow fluctuations. Finally, the jet reversal characteristics with varying freestreams and nozzle pressure ratios are assessed, demonstrating the feasibility and versatility of volumetric velocimetry measurements for industrial aerodynamics.

Nomenclature

f	=	focal length, mm
$f\#$	=	numerical aperture
j_d	=	jet diameter
r	=	reingestion parameter
λ	=	jet-to-freestream momentum ratio
σ_u	=	velocity estimation uncertainty

I. Introduction

AIRCRAFT engine thrust can be redirected by thrust reverser (TR) devices to rapidly decrease the aircraft speed at landing, after touchdown [1,2]. During aircraft operations, the behavior of the TR is critical; when the flow is reversed, the exhaust flow may be reingested, i.e., the circumstance whereby the engine exhaust flow is redirected upstream of the engine and captured again at its inlet. Reingestion must be avoided because it negatively affects the engine lifetime and performance [3–8]. Furthermore, the reversed flow upward or sideward may interfere with control surfaces at the tail segments [1], producing unwanted disturbances to the aircraft control and impairing safety.

Qualitative flow visualization techniques were most commonly adopted in the past to examine these two phenomena because they provide an immediate and intuitive approach to the investigation of the flow topology. Studies using steam injection [1] have shown that the two separate reversed jet plumes rapidly develop into three-dimensional flow patterns. Reingestion resulting from the interaction of the lower jet plume with the ground has also been observed [6]. However, accurate predictions to optimize the TR design and operation require detailed quantitative flow information. At present, the aerodynamic design verification of such systems relies upon a combination of wind-tunnel experiments and numerical simulations.

Most research works that report quantitative measurements of TRs in wind tunnels make use of more traditional techniques, namely, force balance [1–3], pressure [3–5], and temperature measurements. The latter are used as a way to assess the conditions leading to reingestion by (moderate) heating of the jet plume and measurement of the intake flow temperature [4].

Van Hengst [1] made use of surface tufts on the nacelle to study the flow topology induced by the TR and, in particular, the occurrence of flow separation on the rudder. Additionally, the reversed jet plume was visualized by vaporizing liquid nitrogen, as well as by steam injection. Amin and Richards [6] also conducted visualization experiments in a water tunnel, injecting colored dye into the reversed jet; and they compared their results to mist visualizations in the wind tunnel. These methods were effective in delivering a qualitative insight into the overall flow behavior and topology; however, the interpretation of the plume visualizations requires caution, in that the smoke density varies and decays rapidly as a result of turbulent diffusion. Furthermore, the detailed analysis at specific planes of interest is hindered by the fact that only the plume bulk can be inferred. Finally, the comparison among experiments or with data obtained from numerical simulations requires quantitative data to lead to a conclusive investigation.

Early quantitative visualizations of the flow in a TR model were afforded by Bryanston-Cross and Sale [5], who conducted planar particle image velocimetry (PIV) measurements that characterized

Presented as Paper 2022-1945 at the AIAA SciTech Forum, San Diego California and Virtual, January 3–7, 2022; received 24 April 2023; revision received 4 August 2023; accepted for publication 10 September 2023; published online Open Access 19 October 2023.

*Ph.D. Candidate, Aerospace Engineering, Delft University of Technology/Vertical Flight and Aeroacoustics Department, Netherlands Aerospace Centre/NLR; ilda.hysa@nlr.nl.
†Scientist Principal, Vertical Flight and Aeroacoustics Department.
‡Assistant Professor, Aerodynamics Department.
§Professor, Aerodynamics Department.
¶Technical Specialist, Applied Aerodynamics Engineering.
**Technical Specialist, Flight Dynamics Engineering.
††Projects Manager, Projects Department.

the flow leaving the thrust reverser kicker plate. Their measurements indicated the suitability of PIV to investigate this complex flow problem, but they were limited to the state-of-the-art technology of PIV at the time (in 1992).

Over the past decade, PIV has progressed to a reliable whole field measurement technique, which makes it a powerful tool in industrial aerodynamic research. One of the largest stereoscopic PIV systems was employed at NASA, where Wadcock et al. [9] performed measurements in the wake of a full-scale rotor in forward flight, encompassing a field of view (FOV) exceeding 4 m^2. Experiments of comparable scale include those of Jenkins et al. [10], and helicopter rotor wake measurements at the German–Dutch Wind Tunnels (DNW) [11,12]. The study by the DLR, German Aerospace Center (DLR) group [11] involved cameras and lasers in a traversing system that was 10×15 m long. In an aircraft half-model wake measurement by the research group at the ONERA–French Aerospace Lab [13], a 10-camera system with a purpose-built support was employed to cover the entire measurement domain.

Despite its advancements, as indicated by the complexity of these experimental setups, the application of PIV in aeronautics keeps posing a number of challenges: primarily, the region of interest often exceeds the size of the measurement domain due to limitations in illumination and camera resolution. This challenge has been addressed by the introduction of larger, neutrally buoyant tracers: helium-filled soap bubbles (HFSBs) [14]. The superior light scattering of HFSBs as compared to micrometer-size droplets [15] allows planar measurements over several square meters [16] using ordinary PIV illumination and imaging hardware. Such tracers are, however, less abundant in the flowfield; and the resulting images feature a sparse distribution as compared to the experimental conditions of traditional PIV systems based on micrometer-size droplets. At lower levels of the seeding density, the recordings are optimally treated with particle tracking techniques as opposed to cross-correlation analysis. The use of Lagrangian particle tracking [17] is proven effective for the reconstruction of particle tracks in volumes on the order of 1 m^3 [17,18]. In large-scale volumetric Lagrangian particle tracking (LPT) experiments with HFSBs, volume partitioning has often been practiced: Schanz et al. [19] divided a volume of 0.58 m^3 into three parts, with each imaged by a set of cameras. Jux et al. [20] measured a 2 m^3 volume by means of 450 subvolumes, with coaxial volumetric velocimetry and robotic arm manipulation [21]. Recently, Schroeder et al. [22] illuminated a single, large volume (12 m^3) in a closed test room with a massive array of pulsed light-emitting diodes and captured the particle motion with multiple high-resolution cameras.

The application of HFSBs and LPT in industrial wind tunnels is less frequent, given that the time investment for the system setup conflicts with the high operational costs of large wind tunnels. In particular, for such applications, many efforts have been devoted to develop systems able to produce a large amount of HFSBs and distribute them homogeneously and nonintrusively in the wind-tunnel stream [23–25]. Using HFSBs, Faleiros [25] conducted stereoscopic PIV measurements in the wake of a tilt-rotor aircraft at the large low-speed facility (LLF; 9.5×9.5 m^2 test section) of the DNW, encompassing a FOV of 1.1×1.1 m^2. Also, robotic PIV has been demonstrated by Sciacchitano et al. [26] to perform quantitative flow measurements around a turboprop aircraft at the low-speed tunnel (LST; 3×2.25 m^2 test section) of the DNW, covering a measurement volume of 0.15 m^3. Table 1 summarizes the large-scale PIV experiments in industrial/large-scale facilities afforded in the past two decades.

In the present work, large-scale three-dimensional (3-D) measurements are performed that make use of HFSBs as tracers in the LST (DNW) around an aircraft model with engines in the TR configuration. The two main jet plumes resulting from the TR flow have been modeled as a freejet in crossflow (top side) and a confined jet impinging on the ground board (bottom side); and they are discussed under various jet-to-crossflow velocity ratios. Similarities with simplified studies of jets in crossflow [27–31] have been drawn, with the purpose of discussing the large-scale flow organization.

The present objective is to advance the current state of the art of TR flow visualization by introducing large-scale volumetric velocimetry, which allows resolution of the flowfield with higher detail while retaining the advantage of capturing large volumes, which is typical to smoke or steam visualization techniques. The chosen full-field 3-D LPT approach (as opposed to employing traversing systems) significantly decreases the wind-tunnel operation time. A specific challenge of the present experiment is the setup of two separate seeding systems to trace the flow in both the wind-tunnel stream as well as that exhausted by the TR jets. For the latter, a dedicated seeding generator is developed and integrated into the nacelle. The resulting measured flowfields are used to elucidate the full three-dimensional complexity of the flow, illustrating the added value of the measurement technique to the research and development of new aircraft.

II. Experimental Apparatus and Measurement Conditions

A. Wind-Tunnel and Aircraft Model

The experiments were performed in the low-speed tunnel of the German–Dutch Wind Tunnels. The LST is an atmospheric

Table 1 Experiments conducted in industrial or large-scale facilities with PIV

Research group	Wind tunnel	Measurement configuration	Flow tracers	Domain size
Wadcock et al. [9]: rotorcraft wake	NASA Ames Research Center (NFAC) [United States of America (USA)]	Stereo-PIV	Fog	3.99×1.16 m^2
Jenkins et al. [10]: rotorcraft wake	NASA Ames Research Center (NFAC) (USA)	Stereo-PIV	Fog	1.5×0.9 m^2
Coustols et al. [13]: aircraft half-model wake	ONERA, Catapult B10 (France)	2-D PIV, camera moving support system	Fog	1.39×0.92 m^2
Raffel et al. [11]: helicopter rotor trailing vortices	DNW LLF [The Netherlands (NL)]	Stereo-PIV, traversing system	DEHS	0.46×0.36 m^2
De Gregorio et al. [12]: helicopter rotor–fuselage interaction	DNW LLF (NL)	Stereo-PIV, traversing system	DEHS	1×0.35 m^2
Faleiros [25]: tilt-rotor aircraft wake	DNW LLF (NL)	Stereo-PIV, traversing system	HFSB	1.1×1.1 m^2
Sciacchitano et al. [26]: flowfield around turboprop	DNW LST (NL)	Robotic 3-D PIV	HFSB	0.15 m^3
Schanz et al. [19]: turbulent boundary layer on plate	AWM University of Armed Forces Munich (DE)	3-D LPT	HFSB	0.58 m^3
Jux et al. [20]: flow around full-scale cyclist	Delft University of Technology-OJF (NL)	3-D LPT	HFSB	2 m^3
Schroeder et al. [22]: transport of aerosol particles	DLR, closed test room (DE)	3-D LPT	HFSB	12 m^3

NFAC, National Full-Scale Aerodynamics Complex; AWM, Atmospheric Wind tunnel at the University of armed forces Munich; OJF, Open Jet Facility; DE, Germany; DEHS, Di-Ethyl-Hexyl-Sebacate.

closed-return wind tunnel with a contraction ratio of nine. The test section has a width of 3 m, a height of 2.25 m, and a length of 5.75 m. A 1:12-scaled model of a business jet aircraft featuring aft-fuselage-mounted jet engines with bucket-type TRs installed in the test section is shown in Fig. 1. The aircraft model has a total length of 2.092 m with a wingspan of 2.112 m. The pylons and nacelles were designed to allow thrust reversal on the ground. The centerline of the model nacelles was placed at a vertical distance of 0.3 m to the ground board.

The model was installed in the test section with a landing attitude in close proximity to a fixed ground board, where it was attached with three struts, which were adjusted such that the model attitudes were −1.3 deg for pitch and 0 deg for the roll and yaw angle. Flaps were set at a 42 deg angle, and a set of inner wing speed brackets was also in place. The incidence of the horizontal stabilizer was put at its nominal setting of a −2 deg angle. The rudder and elevator angles were set at a 0 deg angle.

B. Engines and TR

The model engines simulated both the inlet and exhaust flows. The latter was generated by compressed air, whereas the inlet flow was controlled via a suction system. The exhaust was reversed by setting the nacelle doors to the TR configuration at angles θ_1 and θ_2, as sketched in Fig. 2. The nacelle length was 520 mm.

For an accurate simulation of the engine flow, the compressed air required to generate the exhaust was heated before being fed into the nacelles. A flow conditioning device was installed in each nacelle, consisting of a throttle plate upstream and downstream of its metal foam disks, with the purpose of homogenizing the exhaust velocity.

The compressed air mass flows to each individual engine were measured with high accuracy via two sonic venturis. The nozzle pressure ratio (NPR) is defined in Eq. (1):

$$\mathrm{NPR} = \frac{p_{t,\mathrm{nozzle}}}{p_\infty} \tag{1}$$

where $p_{t,\mathrm{nozzle}}$ is the total pressure measured with the pressure rake, which was placed slightly ahead of the HFSB rake in order to avoid its contamination; and p_∞ is the static pressure of the freestream. These quantities were measured in real time, and the input voltage to the pressure regulator was set to achieve the desired NPRs. The exhausts were equipped with four rakes, with each containing three total pressure probes and one temperature probe. The rake legs were positioned at azimuth angles of 0, 90, 180, and 270 deg. The inlet ducts of the engines were equipped with six rakes, with each containing four thermocouples, which were used for the reingestion detection. The azimuth angles of the rake legs were 0, 60, 120, 180, 240, and 300 deg. The locations of the thermocouples are shown in Fig. 3. The temperature at each point was measured with an uncertainty of 0.5–1 K, and the averaging measurement time for each point was 10 s. The measured inlet temperatures were used to check for reingestion.

The reingestion parameter r, defined in Eq. (2), is the temperature difference between the total temperature at the engine inlet T_{inlet} (averaged across all inlet rakes) and the freestream total temperature T_∞ normalized by the difference between the mean exhaust jet total temperature T_j (averaged across all exhaust rakes) and the freestream. This parameter is nonzero when reingestion occurs, and it is zero otherwise:

$$r = \frac{T_{\mathrm{inlet}} - T_\infty}{T_j - T_\infty} \tag{2}$$

The chamber aft of the inlet duct was connected to a hole in the pylon through which access was gained to a plenum in the aft end of the fuselage. The inlet mass flows of both the port and starboard engine inlets were routed to this plenum. A Roots-type blower was connected to this same fuselage pipe to generate the suction. A mass flow meter in the suction pipe toward the Roots blower measured the total amount of air sucked.

The experiments reproduced full-scale conditions according to the criteria that the ratio of the momentum of the jet exhaust flow to the freestream flow denoted by λ in Eq. (3) was kept constant between the full scale and the model scale:

$$\lambda = \frac{\rho_j V_j^2}{\rho_\infty V_\infty^2} = \mathrm{const} \tag{3}$$

A simplified description of the flow arrangement is illustrated in Fig. 4. The reversed jets develop across the outer stream in a flowfield

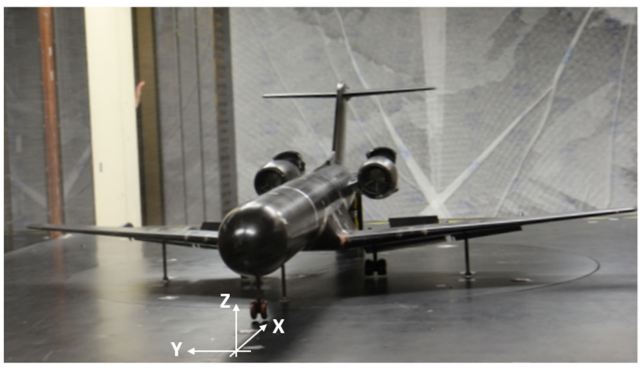

Fig. 1 Aircraft model installed in the DNW LST and system of axes.

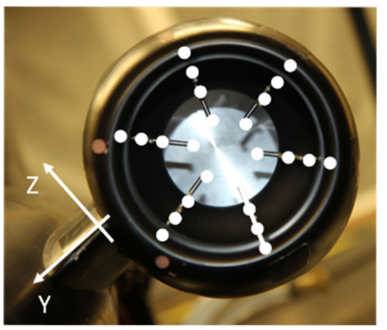

Fig. 3 Photograph of the engine inlet, where the thermocouples' positions are denoted by white circles.

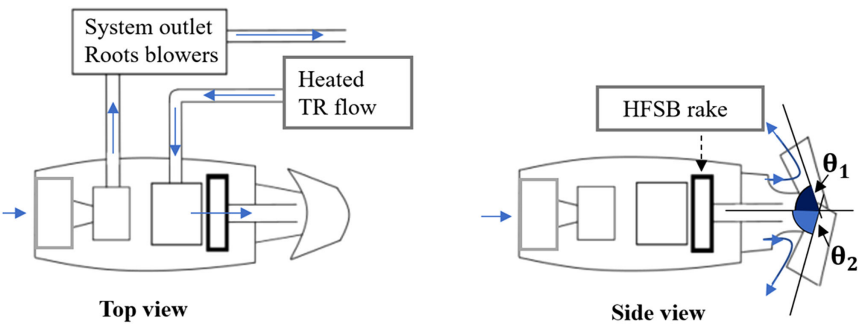

Fig. 2 Schematic representations of engine in TR configuration with air suction at inlet, heated air supply at the exhaust, and HFSB rake installed.

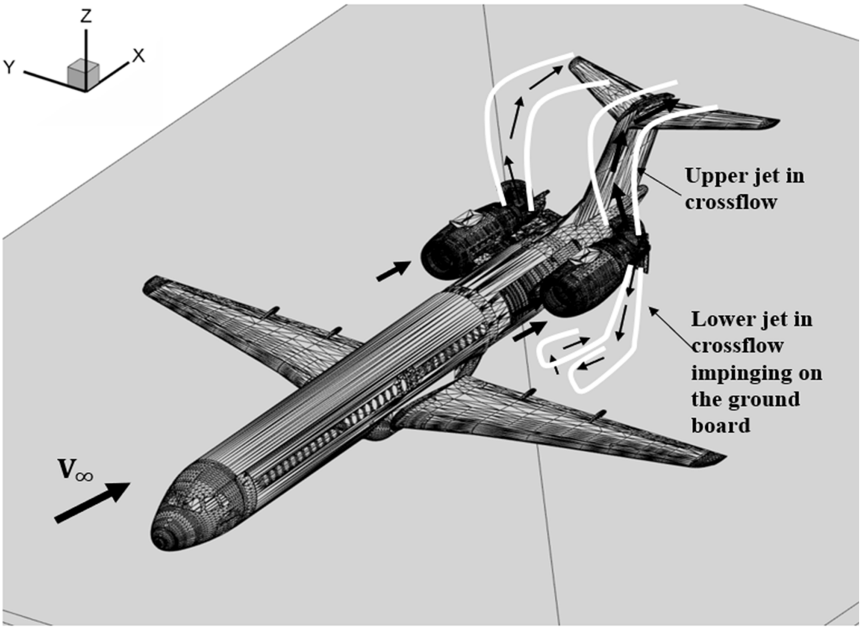

Fig. 4 CAD drawing of the aircraft model and coordinate axis in the origin of the measurement domain. The main flow features are outlined schematically.

that can be approximated as two inclined jets in relative proximity in crossflow. Whereas the upper jet plume is free to propagate upward, the lower jet plume impinges on the ground. Under the assumption of flow symmetry due to a zero yaw angle, the LPT measurements were conducted around only one of the engines.

C. LPT Apparatus and Procedures

In this section, the integration of the large-scale LPT system in the LST wind tunnel is described. Details are given of the seeding systems, the volume illumination, and imaging, as well as the data processing needed to produce the analysis of the time-averaged velocity fields.

1. *Wind-Tunnel Stream Seeding*

Two HFSB seeding systems were used in this experiment. A large seeding rake was used to seed the wind-tunnel freestream; and a small tailor-made rake was used to seed the TR jet emanating from the engine exhaust.

The freestream seeding rake comprised 10 wings, each with 20 HFSB generators, with a total of 200 HFSB generators. The generators were designed and Computer Numerical Control (CNC)-manufactured at the Dutch Aerospace Center/NLR (NLR). A schematic of the nozzle of one of the generators is given in Fig. 5, and its main dimensions are summarized in Table 2.

The NLR design of the nozzle consists of a conical contraction region upstream of the orifice (beta >90 deg) in order to avoid flow separation at the junction between the cylindrical part and the end of the wall, where residues of recirculating soap fluid may accumulate under specific conditions.

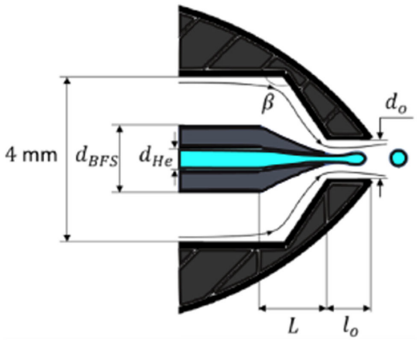

Fig. 5 Schematic section view of the bubble generators used in the experiments. Sketch adapted from Ref. [23].

Table 2 Dimensions of NLR generator

Parameter	Value
β	125 deg
d_{BFS}	2 mm
d_{He}	0.6 mm
d_o	1 mm
L	2 mm
l_o	1 mm

The bubbles are introduced into the flow downstream of the tunnel's turbulence screen in order to avoid contaminating them. They are introduced in the settling chamber so that most of the flow interference caused by the rake decays along the wind-tunnel contraction [25]. The system releases tracers at a rate of 5×10^6 tracers/s with median diameter of 0.45 mm.

A photograph of the seeding rake placed in the settling chamber of the DNW's LST is shown in Fig. 6. The ratios of the rates of the supply of air, helium and soap were controlled following [23] in order to ensure the neutral buoyancy of the tracers. The two separate rakes were connected to the same FSU. The helium supply line was pressure controlled, and the mass flow was monitored. The compressed air supply line was mass flow controlled. The soap flow was regulated by controlling the pressure of the soap tank and monitoring the mass flow using the Mini Cori Flow from Bronkhorst. The soap solution used was SAI 1035 from Sage Action, Inc. A particle filter was implemented in the soap supply line to prevent blockage of the mass flow meter or the flow restrictors. Digital pressure sensors were connected to the fluid supply lines at the freestream seeding rake in the settling chamber to remotely monitor for possible leakage.

2. *Engine Flow Seeding*

To seed the jet exiting the thrust reverser, a HFSB seeding rake was designed for the isolated nacelle. It is equipped with eight bubble generators (total production rate $\sim 0.2 \times 10^6$ tracers/s) mounted in an aerodynamically shaped 3-D-printed support. The rake was positioned such that the exit plane of the generators was slightly

Fig. 6 Wind-tunnel seeding rake installed in the settling chamber.

downstream of the internal total pressure rakes to prevent total pressure rakes being contaminated by soap. Figure 7 shows a photograph of the internal seeding rake and its installed position inside the nacelle.

Measurements were performed with different seeding conditions. First, experiments only seeding the engine jet were performed to visualize the trajectory of the exhaust bulk flow and compare them with temperature-based reingestion detection. Later experiments with the seeded freestream were made to quantify the interactions between the TR flow and the freestream.

3. Volume Illumination

A Quantel EverGreen EHP30 (Neodymium-doped Yttrium Aluminum Garnet, Nd:YAG laser, 300 mJ/pulse) laser was used as an illumination source. The laser was illuminating the volume from approximately the same direction as the cameras. The laser beam was first expanded with a spherical lens and further sent through a beam diffuser. The laser was mounted on an X95 beam outside of the test section.

This light source provided enough illumination intensity to cover a volume in excess of 1 m^3 when using HFSBs. The laser was operated in double-pulse mode at a frequency of 10 Hz, with pulse separation ranging from 140 to 400 μs, depending on the flow speed.

4. Imaging and Recording

Three scientific complementary metal-oxide-semiconductor cameras (PCO.Edge 5.5) were used to record the light scattered by the tracers within a measured volume of approximately 0.5 m^3. Although it is possible in theory to perform 3-D particle reconstruction with only two cameras, most volumetric PIV/Particle Tracking Velocimetry (PTV) experiments involve three or four cameras in order to minimize false particle reconstructions [32]. The choice of three cameras (instead of four) was done in favor of simplicity, and it was possible in this case due to the particle concentration being below 0.1 particles per pixel (see Sec. II.C.5 for more details on particle concentration). At higher seeding densities, more than three cameras might be necessary for accurate 3-D particle reconstruction.

The dimensions of the measurement domain, along with the respective positions of the cameras and the laser, are illustrated in Fig. 8. The cameras were arranged in a two-dimensional (2-D) configuration, and they were mounted on X95 beams outside of the test section, spanning the plane highlighted with blue in the sketch. The total aperture of the

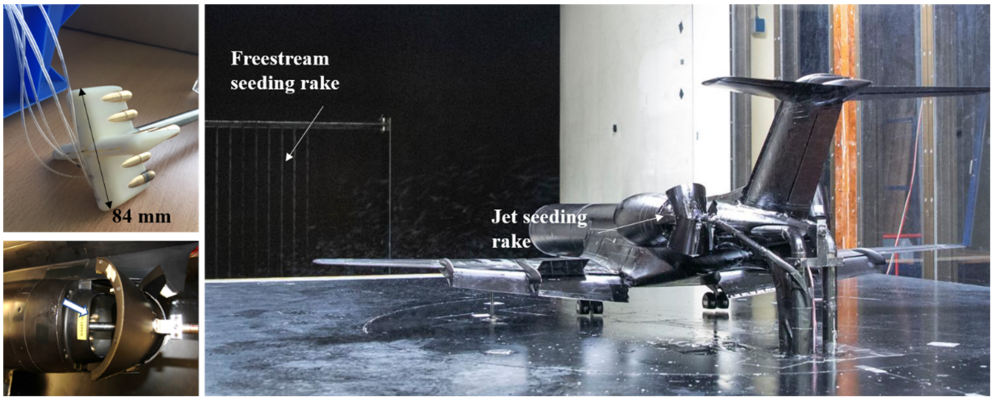

Fig. 7 Internal jet seeding rake dimensions (top left), position of the rake after installation in the engine (bottom left), and overall view of the wind-tunnel model with the freestream and the jet seeding rakes (right).

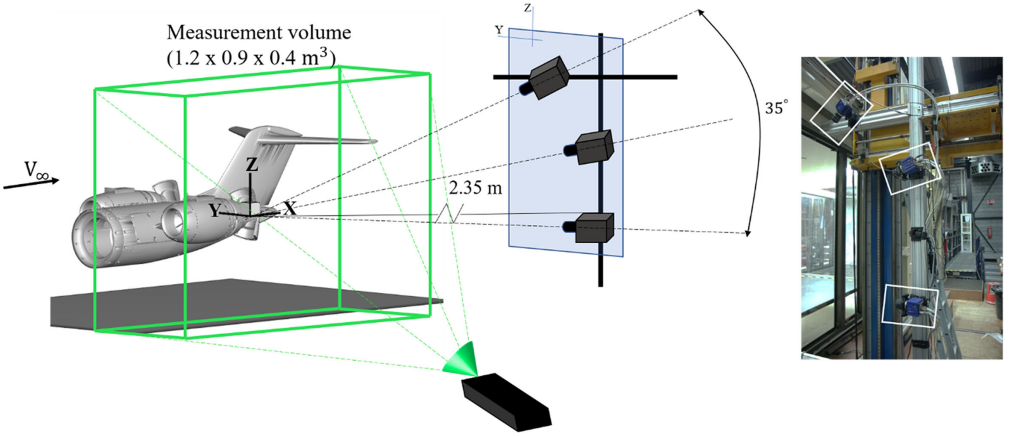

Fig. 8 Schematic illustration of illumination and imaging layout (left). The measurement volume is highlighted in the green box. The laser and the cameras are on the same side of the model. The orientation axis is centered at the origin of the PIV measurement volume. Photograph of the cameras installed outside of the test section (right).

system is 35 deg. The measurement volume in the streamwise extent covers the engine inlet, the thrust reverser, and the aircraft tail. In the vertical direction, the volume encompasses the ground and the horizontal stabilizer. An overview of the imaging parameters is given in Table 3.

The arrangement of the laser and cameras results in some regions without optical access due to shadows. The shadows result from the TR doors and the wing. Additionally, the nacelle casts a shadow in the region between the nacelle and the fuselage. The model was completely painted in black; however, some reflections did result: most notably around the engine inlet and in the TR doors due to accumulation of soap, as can be seen in Fig. 9 (left).

The geometrical image of HFSB tracers covers approximately 1.4 pixels in the images. The small angle between illumination and imaging causes the two glare points, characteristic of the HFSB imaging, to merge into a single one [25]. The final diameter of this single glare point is approximately 3 pixels; this is mostly as a result of diffraction. Image preprocessing was applied to improve the detectability of particle images for the LPT analysis, with the resulting images and a close-up of the particles shown in Fig. 9 (right).

The image processing steps that were performed for the purpose of eliminating background reflections to maximize the amount of detected particles are as follows: minimum pixel intensity subtraction over time (with a filter length of seven recordings); sliding spatial minimum intensity subtraction based on a neighborhood of 7×7 pixels; intensity normalization based on a local intensity averaged over a window of 150×150 pixels. Finally, the intensity of each frame was normalized to the first frame.

5. *Data Processing*

For the measurements conducted with seeding in the freestream, a total of approximately 200,000 particles are captured in each recording (particle image density of 0.05 particles per pixel), corresponding to a tracers' concentration of 0.5 particle/cm^3. About 75.000 of the detected particles are accepted into valid tracks. In the freestream, a particle is displaced of approximately 5 pixels between the two frames. The particles' 3-D positions are obtained with the iterative particle reconstruction (IPR) algorithm [32] and tracked using the shake-the-box algorithm [17] tailored to two-pulse recordings [33] implemented in LaVision DaVis 10.1.2 software [34]. The instantaneous velocity is obtained at scattered locations and converted to a Cartesian grid over cubic cells of 1 cm^3. Each velocity sample falling within the cell forms an ensemble yielding the time-averaged velocity vector at the cell center. The measurement domain encompasses $120 \times 40 \times 90$ cm^3, and the velocity is described with a grid of $230 \times 80 \times 181$ nodes (adjacent cells overlap by 50%) and 5 mm vector spacing. With this 10 mm bin size, and the recording frequency of 10 Hz, biases associated with the ensemble binning scheme (such as double counting of particles) take effect in regions with an absolute value of velocity below 0.01 m/s. Most of the low-speed regions of interest (such as the wake of the jet) feature higher velocities; overall, the number of bins with velocities lower than 0.01 m/s comprise less than 1% of the domain volume. Therefore, this is not considered to be a significant factor in this measurement.

Every bin comprises approximately 5000 samples; however, the concentration varies across the measurement domain. A criterion of at least 50 valid data tracks per bin is set. At these conditions, the bin size is 1/10th of the jet diameter. A measurement of the dynamic spatial range [35] of 120 is attained from the ratio between the largest and smallest measurable scales.

The measurement accuracy is evaluated via the dynamic velocity range (DVR) [36], which is defined as the ratio between the maximum and minimum resolvable levels of velocity. In the present case, the maximum velocity occurs at the jet centerline. For the minimum resolvable velocity, an estimation of the velocity uncertainty is required. Following Ref. [37], the measurement uncertainty is statistically determined by the ratio between the relevant velocity fluctuations (axial and vertical velocities' standard deviations in this case) and the square root of the amount of samples per bin. In the regions of the jet core, where the highest turbulent fluctuations were recorded, the measurement uncertainty is approximately 0.4% of the maximum measured velocity. In the rest of the domain, this value is below 0.1%. Taking an average value of u' and N_p across the domain results in DVR = 200.

For the purposes of flow topology visualization and reingestion, detection measurements with jet seeding only were conducted. For these measurements, there were (on average) 20.000 particles continuously tracked between the two frames. The bin size for the averaging was chosen to be 20 mm with 75% overlap in order to achieve velocity convergence with reduced particle density. Approximately 1200 particles were sampled per bin (in the region of the seeded domain). The measurement uncertainty was in the order of 0.6% of the peak measured velocity in the seeded domain. This uncertainty increased to up to

Table 3 Summary of imaging parameters

Parameter	Value
Laser pulse separation, μs	Double Δt: 150, 400
Recording frequency, Hz	10
Sensor size, pixels	2560×2160
Image sensor pixel pitch, μm	5.6×5.6
Magnification	0.018
Objective focal length, mm	35
Numerical aperture	5.6
No. of recordings	250
Measurement volume, m^3	1.2 (X) $\times$ 0.4 (Y) $\times$ 0.9 (Z)

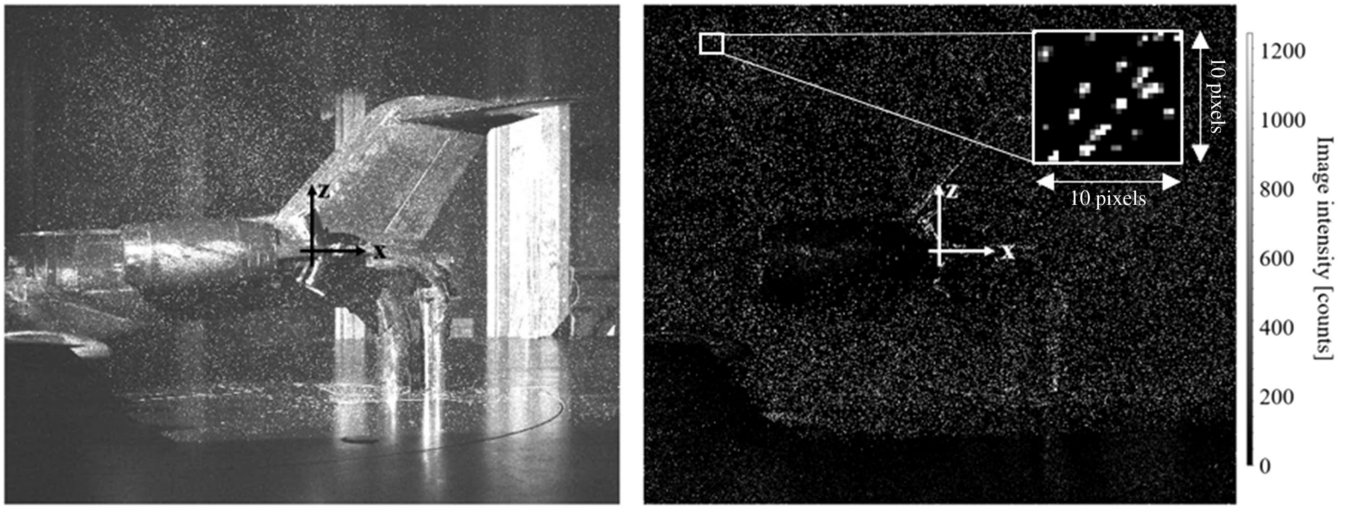

Fig. 9 Raw image from camera 3 (left). Same image after preprocessing (right; counts refer to both images).

1% in the limits of the domain due to the reduced seeding in these regions.

It is important to note that even though the tracking technique is called Lagrangian particle tracking, the two-pulse measurement does not allow for the reconstruction of long Lagrangian trajectories in time. This is particularly relevant to keep in mind with regard to the reingestion detection results shown in the next section. Reingestion identification was accomplished by inference on the presence of particles in regions close to the engine inlet, rather than by following particular trajectories from the exhaust back to the inlet.

Further analysis of the time-averaged binned velocity vector fields is performed in Tecplot 360 EX R2, where the volumetric flowfield data are overlaid onto the computer-aided drawing (CAD) geometry of the wind-tunnel model.

III. Experimental Results and Analysis

A. Global Flow Topology

The time-averaged velocity fields obtained with the two different seeding strategies (i.e., homogeneous seeding and jet-only seeding) are shown in Fig. 10 next to a photograph taken during a visualization experiment produced with steam injection at a comparable freestream velocity and NPR ($V_{\text{jet}}/V_\infty = 2.5$). The steam visualization was obtained on the same aircraft model but employed a different thrust reverser configuration. Therefore, the goal is not one-to-one comparison; rather, it is the presentation of the advancement that quantitative flow visualization offers over the qualitative state of the art. The streamlines extracted from the velocity field results elucidate a number of flow features. Initially, the jet plumes propagate in the direction set by the TR door orientation before bending downstream due to momentum exerted on them by the freestream flow. Behind the jet, a quasi-stagnant region is created in which the horizontal tail and the control surfaces are immersed. The lower jet plume is obstructed by the ground plane, as was also seen in the steam visualization. A separation bubble is observed, where the incoming boundary layer separates under the effect of the increased pressure at the jet stagnation point. This recirculation region is identified as the primary mechanism for jet plume reingestion. With the NPR increase, the separation bubble size will also increase until the point (part) of the jet plume is reingested into the inlet.

As discussed in previous studies [27–30], the interaction of a jet impinging on a flat surface has a complex flowfield. In these works, planar PIV in the midplane through the jet, laser doppler velocimetry, and quantitative flow visualizations were employed to study the jet properties in simplified conditions. The principal factors affecting the resulting flowfield properties were identified as the nozzle shape, the jet-to-crossflow velocity ratio, the nozzle-to-ground-plate distance, the presence of confinements, the number of jets, and their relative proximity. The variation of these factors was studied, and the flow was typically divided in a number of characteristic regions [27]. For the study at hand, the two jet plumes coming out of the TR can be understood as follows: the top plume as a free inclined jet expanding into crossflow, and the lower one as an inclined jet in crossflow impinging on a ground plate. Here, the distance to the ground plate is fixed to the landing configuration distance, and so is the TR door shape. The factor that was varied is the jet-to-freestream velocity ratio. The current case is made more complex by the TR door geometry; the presence of distortions upstream in the crossflow due to the presence of the wing, fuselage, and nacelle; and the inclination of the jet to the freestream, as outlined in Fig. 5. Additionally, the NPR and freestream velocity conditions in Refs. [27–31] are significantly different, and so the goal in this section is not direct quantitative comparison; instead, it is revealing the large-scale structures present in the flow.

Following Nguyen et al. [28], the jet plume is roughly separated in three regions, as illustrated in Fig. 11. These include a region where

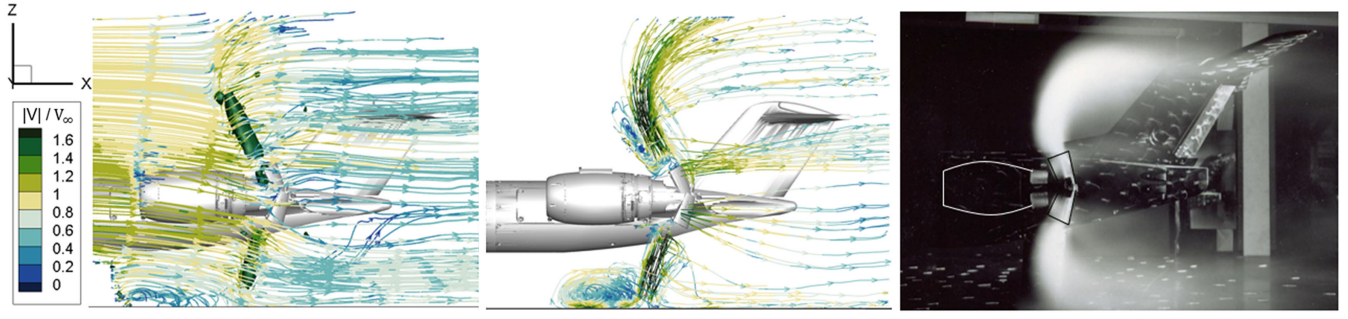

Fig. 10 Time-averaged velocity field from the LPT measurement visualized with color-coded streamlines' homogeneous domain seeding (left), same point with jet seeding only (middle), and reversed jet visualized with steam (right; nacelle and TR doors have been highlighted).

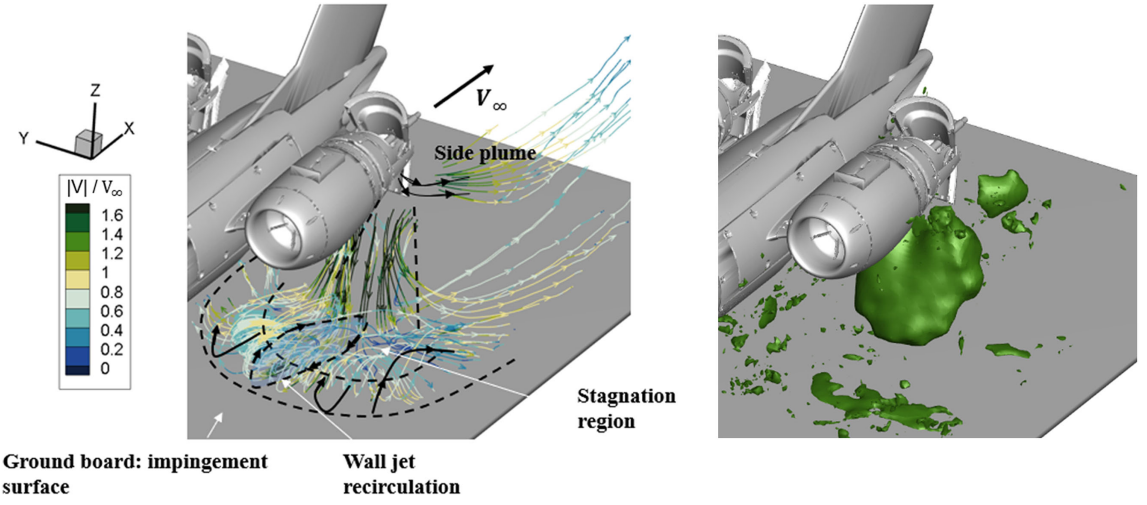

Fig. 11 Lower jet flow structures visualized with streamlines (left). The rest of the flowfield has been omitted for clarity. Velocity magnitude isosurface at $V/V_\infty = 1.3$ (right).

the flow behaves like a freejet; an impingement region, where the flow structure is affected by the presence of the impingement plane; and a wall jet region, where the flow develops in the radial direction along the impingement surface. This wall jet is then observed to recirculate in vortical structures, similar to what was observed by Barata et al. [27], although different in magnitude. For the investigation of exhaust reingestion, the propagation of the wall jet upstream of engine intake as well as the extent of the recirculation region above the ground plane are critical.

Additional to the main jet plume, secondary small plumes are captured by this experiment, i.e., flow leaking from the side of the TR door close to their hinge point. Such side plumes are also reported from the previous steam visualizations of Van Hengst [1]. They can be clearly observed on the outer side of the engine (negative y direction); however, it is not possible to observe the occurrence of this side plume on the side of the fuselage due to limited optical access and the shadow of the engine on that side.

In multijet impingement studies [27,30], it is reported that the jets of the two operational engines will interact with each other, establishing a plane of symmetry in between on which the flow topology is mirrored. Inspection of the flow topology from the rear of the airplane, as depicted in Fig. 12, shows that the wall jet recirculation is asymmetrical, having a smaller radius and a higher vertical velocity component magnitude on the side next to the fuselage. This is explained by a stagnation region in the symmetry plane near the ground surface, which is created at the locations where the two wall jets impinge onto each other. The "free side" of the recirculation bubble, on the other hand, is wider and with lower vertical velocity components. The wall jet is only lifted from the surface and is then deflected downstream further in the x direction, as can be more clearly seen in Fig. 10 (left).

In contrast to the lower plume, the upper plume is unobstructed, slowly reorienting in the streamwise direction by the exerted momentum of the freestream flow. The flowfield of the upper jet can be divided into four regions: the jet–crossflow interface, the jet core, the jet wake, and the flow leakage from the gap between the TR doors, illustrated in Fig. 13. The jet–crossflow interface constitutes a stagnation region, which is also seen on the right, where streamlines around the centerplane through the jet emanating from the freestream region have been plotted (the jet has been omitted for better visibility). It can be seen that the freestream is deflected around the jet sideways, up to the point denoted by the arrowhead: at which point, the flow starts to get deflected upward.

The upper plume flow is of no relevance for flow reingestion. However, it can play a role in the controllability of the aircraft due to the possible interaction with the rudder. Particularly in cases of landing with a sideslip angle, the plume hitting the rudder can be detrimental to aircraft control [1,3,4]. In the conditions with 0 deg sideslip that are measured in this experiment, this situation is not observed in any of the measured points. However, it is seen that the pitch control surfaces (elevators and horizontal tail) are immersed in the wake of the jet.

To quantify to what extent the local velocity ahead of the tail is altered by the presence of the plume, an effective angle of attack of the tail is be defined as

$$\alpha_{\text{effective}} = \alpha_i + \alpha_g \tag{4}$$

where the angle of the local flow over the tail α_i and the geometrical angle of the horizontal stabilizer α_g are shown schematically in Fig. 13 (right). As noted in Sec. II, the horizontal tail is set at α_g fixed at -2 deg. Also, α_i is calculated from the atan (w/u) ahead of the tail. This angle is rather small (less than 0.1 deg) in all conditions, except for the two with the highest λ [Eq. (3)]. In the condition of $\lambda = 35$, the incoming flow to the horizontal tail is at approximately 3 deg, resulting in an effective of attack $\alpha_{\text{effective}}$ of 1 deg. For the case of $\lambda = 24$, the incoming flow is oriented at 1.8 deg, resulting in an approximately 0 deg effective angle.

The core region of the jet is characterized by a maximum jet velocity along the centerline with a bell-shaped mean velocity profile. This is illustrated in Fig. 14, which shows the time-averaged velocity profile and the standard deviation of the axial and radial velocity components extracted along the line denoted across the jet core in Fig. 13 (left). Here, a local coordinate along the jet-normal direction is normalized by the jet exit diameter j_d (determined by the geometry of the engine).

The velocity fluctuations along the axial and radial directions are on the order of 100% of the freestream velocity values. This is not typical of fully developed top-hat profile jets where the fluctuations are small in the core and peak in the shear layers around the edges [28]. Instead, this jet is unsteady and fluctuating strongly along the entire jet diameter.

Additional flow features such as the flow leakage between the deployed TR doors are observed. This is the flow escaping from a gap in between the deployed TR doors and relates to TR efficiency considerations due to the fact that the amount of flow effectively

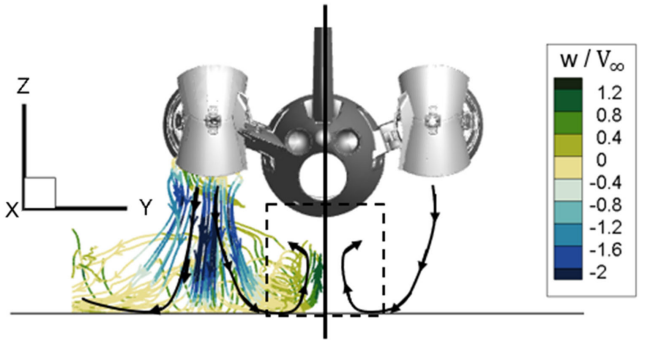

Fig. 12 Back view of the lower jet visualized with streamlines. The region where interactions between the two jets is expected is outlined in the dotted box, and the plane of symmetry along the x-z plane is denoted with the black line.

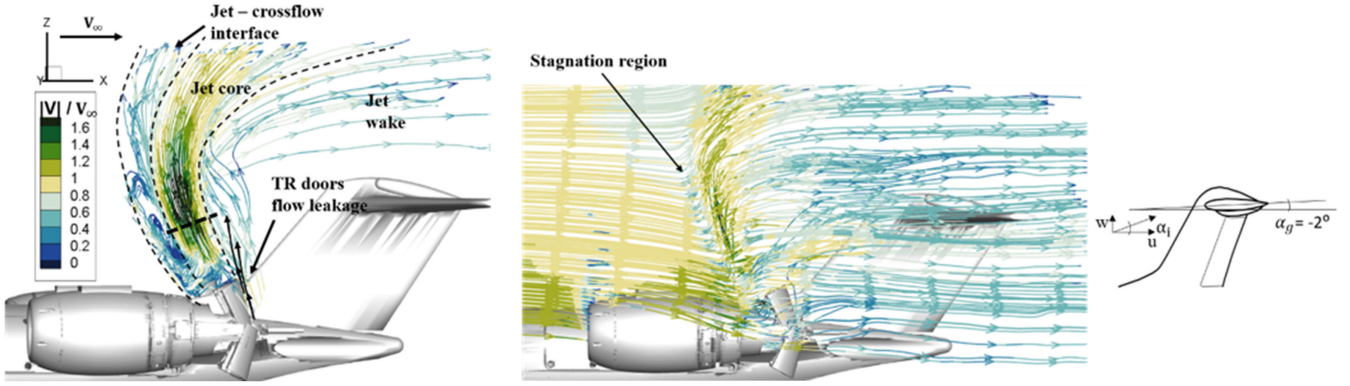

Fig. 13 Top jet plume regions visualized with streamlines (left). Freestream flow deflection around the jet (middle). Schematic of the local flow over the horizontal tail (right).

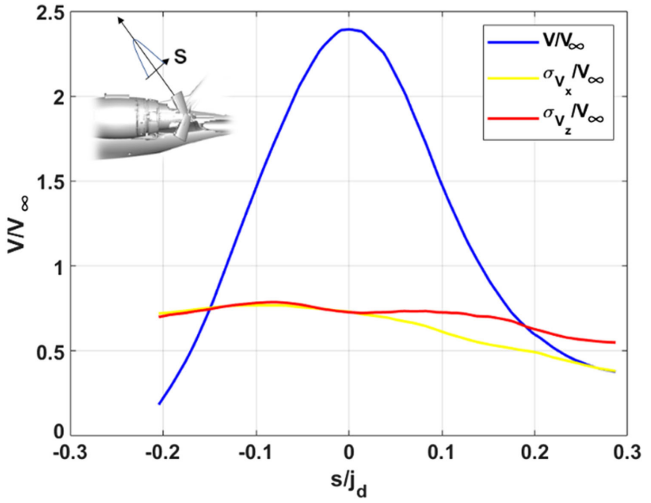

Fig. 14 Velocity magnitude profile of the jet core, along with the axial and radial velocity fluctuation components.

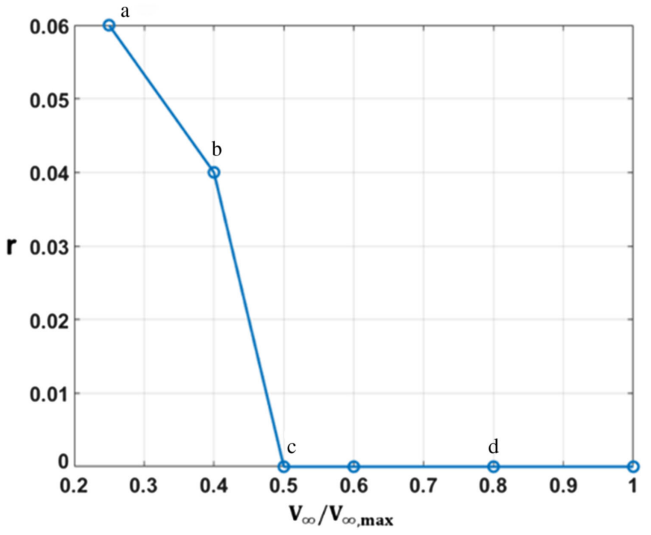

Fig. 15 Temperature rake reingestion parameter vs freestream velocity. Cases a, b, c, and d correspond to the cases in the velocity contour plots of Fig. 16.

reversed is decreased by these leakages. For the current TR model, the area of this gap measured from the TR geometry is approximately 5% of the total opening area for flow reversal.

B. Comparison with Temperature-Based Reingestion Detection

Reingestion detection measurements with temperature rakes have been conducted for a velocity sweep with a fixed NPR (which was the highest NPR tested because it is the most critical for reingestion). The reingestion parameter *r*, as defined in Eq. (2), is zero for cases where no reingestion is detected and positive otherwise, with a higher value suggesting larger parts of the plume are reingested. These results are plotted in Fig. 15.

The LPT measurements for the same velocity sweep have been plotted in the midplane through the nacelle in Fig. 16, where each condition is directly compared to the temperature results. Measurements with jet seeding were considered in order to unambiguously detect the presence of particles originating from the jet. Therefore, in the interpretation of the results, the presence of particles at the engine inlet or ahead of it is taken as evidence of reingestion.

It can be seen that these time-averaged results show good agreement. As discussed in the previous section, the mechanism that gives rise to reingestion is the recirculation of the wall jet resulting from the lower plume impinging on the ground board. The sizes of these recirculation regions in both the axial as well as the vertical directions are critical in terms of closeness to the engine inlet.

In both conditions a and b, it appears that the recirculation extends further upstream under the wing; but due to the shadows of the wing (as well as the fact that this region is in the limit of the domain), the measurement there is not available.

The magnitude of reingestion is also in agreement between the temperature measurements and LPT, whereby the higher reingestion parameter corresponds to a higher number of particles detected. The rest of the points have zero reingestion. The LPT measurements confirm this. In point c, the size of the recirculation bubble is considerably smaller, and it does not seem to approach the inlet on average; and in point d, the freestream-to-jet momentum is increased to the point that the forward propagation of the jet is minimal.

The LPT results can be seen as complementary to the temperature measurements, in that they elucidate the aerodynamics leading to reingestion.

C. Parametric Analysis with NPR and Momentum Ratio

In this section, the results of measurements with varying conditions are presented: a flow topology variation with a freestream velocity sweep at a fixed NPR, and the jet profile variation with the NPR sweeps at two different freestream velocities.

The two main jet plumes and the side plumes have been visualized with velocity isosurfaces and plotted for a velocity sweep in Fig. 17. The value taken to obtain the isosurfaces is varied for each condition for better visibility. The jet-to-freestream momentum is increasing from left to right (as the freestream velocity decreases): as expected, so is the forward propagation of the jet. It can also be observed that the

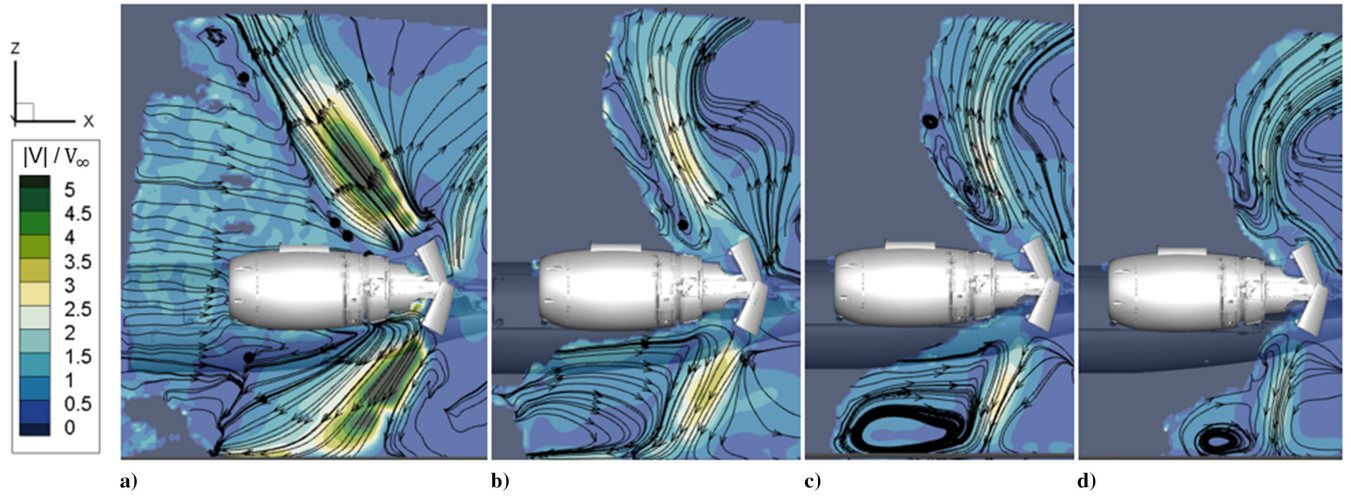

Fig. 16 Normalized velocity contours and surface streamlines in the midplane through the nacelle. Freestream velocity increases from left to right, and NPR is fixed. Regions with no vector information are a result of limited particle count from the jet seeding.

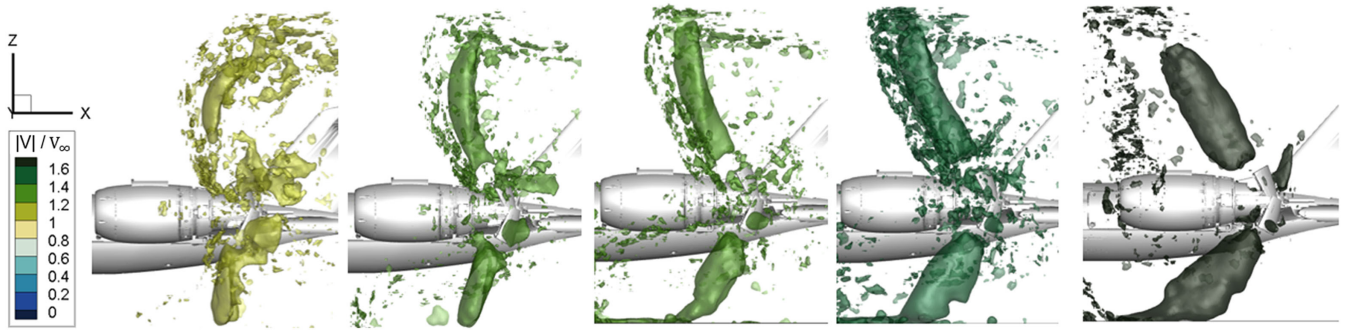

Fig. 17 Velocity isosurfaces for increasing V_{jet}/V_∞ (left to right).

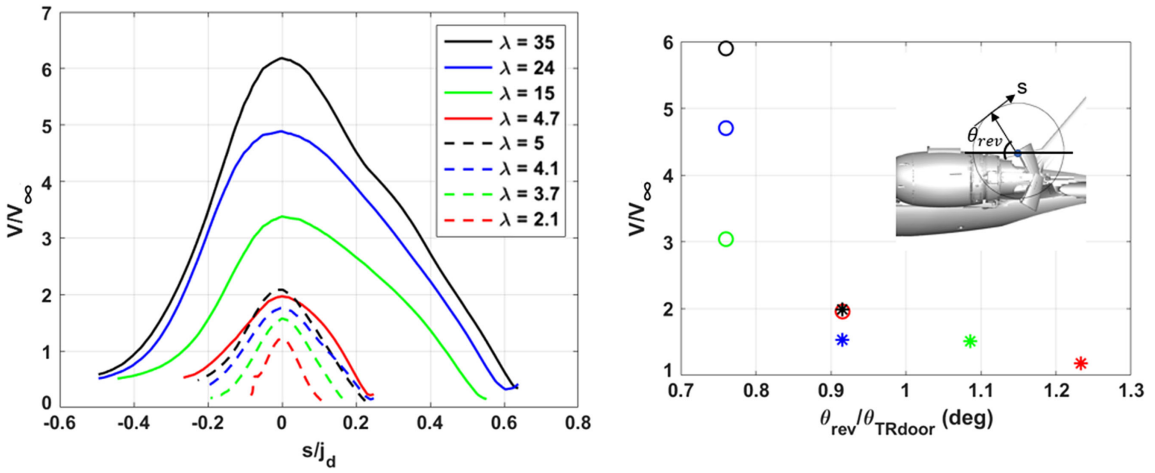

Fig. 18 Jet mean velocity profiles for measurements featuring NPR sweeps at two different velocity freestream values.

jet diameter increases in this direction; i.e., the jet expands more when V_{jet}/V_∞ is higher, and it is thinner otherwise.

Additionally, measurements with NPR sweeps at two fixed freestream velocities have been performed. Here, seven different NPR values are plotted in Fig. 18 with conditions of V_{jet}/V_∞ varying from 1.5 to six. The legend of the graph on the left denotes the jet momentum-to-freestream ratio λ as defined in Eq. (3). The dashed lines represent the first NPR sweep at $V_{\infty,1}$, and the solid lines represent the second NPR sweep at a lower freestream speed of $V_{\infty,2} = 0.4V_{\infty,1}$. The jet profiles are extracted normal to the jet for all the different conditions along a constant radial distance from the top TR door.

Not only the jet velocity but also its orientation vary with the different conditions. This is shown in Fig. 18 (right), where the angle that the jet centerline makes with the horizontal is normalized with the angle of the upper TR door and plotted. The color coding matches the conditions on the left, with the solid circles corresponding to the solid lines, and the asterisks corresponding to the dashed lines.

It can be observed that as the jet-to-freestream momentum increases, the jet is more strongly reversed, as is to be expected. The last two conditions (green and red dashed lines and the asterisk angle) correspond to effectively no jet reversal. The jet does not propagate forward but is defected downstream under these conditions, as demonstrated by the fact that the angle it makes with the horizontal is larger than the geometrical angle of the TR door. It can also be observed that conditions with different velocities and NPRs but a very similar momentum ratio ($\lambda = 5$ and $\lambda = 4.7$, denoted by the black dashed line and the red solid line) likewise have an almost identical velocity distribution as well as deflection angle, which is in line with the scaling theory.

IV. Conclusions

A quantitative flow visualization technique was successfully demonstrated for the investigation of thrust reverser flows in an industrial wind-tunnel environment. The large-scale volumetric velocimetry measurement was made possible by employing helium-filled soap bubbles as flow tracers. Flow seeding was achieved with two separate seeding rakes: one integrated inside the nacelle, and one in the wind-tunnel settling chamber. The need to introduce particle tracers in the engine exhaust flow complexifies the implementation of this kind of measurement; in this case, it was dealt with by employing a small HFSB generator array that was tailor made to fit the engine nacelle. The most effective visualization strategy was found to perform measurements with jet-only seeding, alongside the jet and freestream flow seedings.

Testing was completed in typically 3–5 min per condition, following a full-field approach, as opposed to scanning the domain, where the time needed for the measurements is multiplied by the number of scanning planes/volumes.

The wind-tunnel experiments were conducted at the DNW LST on a 1:12-scaled thrust reverser, which is part of a full aircraft model. A measurement volume of 0.5 m^3 was attained, capturing the full complexity and three-dimensionality of the flowfield. Employing Lagrangian particle tracking, a quantitative assessment of the flow velocity was achieved, with a vector resolution of 1 cm. A key advantage over classical flow visualization techniques is that the flowfield may be studied at specific planes and from various perspectives. Several flow features were elucidated, such as flow reversal, jet plume recirculation due to ground effect, flow leakage, and reingestion.

In conclusion, large-scale velocimetry offers key insights into the flow features that lead to reingestion, and it is complementary to the inlet temperature-probe-based detection criterion.

References

[1] Van Hengst, J., "Aerodynamic Integration of Thrust Reversers on the Fokker 100," *Aerodynamic Engine Airframe Integration for High Performance Aircraft and Missiles: Papers Presented and Discussions Held at the Fluid Dynamics Panel Symposium Held, AGARD 498*, Vol. 10, 1991, pp. 129–138.

[2] Strash, D. J., Summa, J. M., Frank, J. H., and Standish, R., "Aerodynamic Analysis of an Installed Thrust Reverser," *33rd Joint Propulsion Conference and Exhibit*, AIAA Paper 1997-3153, 1997. https://doi.org/10.2514/6.1997-3153

[3] Asbury, S., and Yetter, J., "Static Performance of a Wing-Mounted Thrust Reverser Concept," *34th AIAA/ASME/SAE/ASEE Joint Propulsion Conference and Exhibit*, AIAA Paper 1998-3256, 1998. https://doi.org/10.2514/6.1998-3256

[4] Burgsmueller, W., Castan, C., Kooi, J., and Becle, J., "Recent Developments in Low-Speed TPS-Testing for Engine Integration Drag and Installed Thrust Reverser Simulation," *Aerodynamic Engine Airframe Integration for High Performance Aircraft and Missiles: Papers Presented and Discussions Held at the Fluid Dynamics Panel Symposium, AGARD 485*, Vol. 10, 1992, Paper 15, pp. 113–127.

[5] Bryanston-Cross, P., and Sale, R., "The Quantitative Visualization of the Flow in a 1/10th Scale Model Thrust Reverser at the Aircraft Research Association, Bedfort," *International Gas Turbine and Aeroengine Congress and Exposition*, American Soc. of Mechanical Engineers, Fairfield, NJ, 1992. https://doi.org/10.1115/92-GT-233

[6] Amin, N. F., and Richards, J., "Thrust Reverser Exhaust Plume Reingestion Model Tests," *Journal of Aircraft*, Vol. 21, No. 6, 1984, pp. 401–407.

[7] Schnurr, N. M., Williamson, J. W., and Tatom, J. W., "An Analytical Investigation of the Impingement of Jets on Curved Deflectors," *AIAA Journal*, Vol. 10, No. 11, 1972, pp. 1430–1435.

[8] Sarpkaya, T., and Hiriart, G., "Analysis of Curved Target-Type Thrust Reversers," *AIAA Journal*, Vol. 13, No. 2, 1975, pp. 185–192.

[9] Wadcock, A. J., Yamauchi, G. K., Solis, E., and Pete, A. E., "PIV Measurements in the Wake of a Full-Scale Rotor in Forward Flight," AIAA Paper 2011-3370, 2011. https://doi.org/10.2514/6.2011-3370

[10] Jenkins, L. N., Yao, C. S., Bartram, S. M., Harris, J., Allan, B., Wong, O., and Mace, W. D., "Development of Large Field-of-View PIV System for Rotorcraft Testing in the 14-x 22-Foot Subsonic Tunnel," *AHS international 65th Forum and Technology Display*, Vertical Flight Soc., Grapevine, TX, 2009.

[11] Raffel, M., Richard, H., Ehrenfried, K., Van der Wall, B., Burley, C., Beamier, P., McAlister, K., and Pengel, K., "Recording and Evaluation Methods of PIV Investigations on a Helicopter Rotor Model," *Experiments in Fluids*, Vol. 36, Jan. 2004, pp. 146–156. https://doi.org/10.1007/s00348-003-0689-7

[12] De Gregorio, F., Pengel, K., and Kindler, K., "A Comprehensive PIV Measurement Campaign on a Fully Equipped Helicopter Model," *Experiments in Fluids*, Vol. 53, July 2012, pp. 37–49. https://doi.org/10.1007/s00348-011-1185-0

[13] Coustols, E., Jacquin, L., Moeens, F., and Molton, P., "Status of ONERA Research on Wake Vortex in the Framework of National Activities and European Collaboration," *ECCOMAS*, 2004.

[14] Scarano, F., Ghaemi, S., Caridi, G., Bosbach, J., Dierksheide, U., and Sciacchitano, A., "On the Use of Helium-Filled Soap Bubbles for Large-Scale Tomographic PIV in Wind Tunnel Experiments," *Experiments in Fluids*, Vol. 56, Feb. 2015, Paper 42. https://doi.org/10.1007/s00348-015-1909-7

[15] Caridi, G. C. A., Ragni, D., Sciachittano, A., and Scarano, F., "HFSB-Seeding for Large-Scale Tomographic PIV in Wind Tunnels," *Experiments in Fluids*, Vol. 57, No. 11, 2016, Paper 190. https://doi.org/10.1007/s00348-016-2277-7

[16] Spoelstra, A., Norante, L. M., Terra, W., Sciacchitano, A., and Scarano, F., "On-Site Cycling Drag Analysis with the Ring of Fire," *Experiments in Fluids*, Vol. 60, June 2019, pp. 1–16. https://doi.org/10.1007/s00348-019-2737-y

[17] Schanz, D., Gesemann, S., and Schroeder, A., "Shake-The-Box: Lagrangian Particle Tracking at High Image Densities," *Experiments in Fluids*, Vol. 57, May 2016, pp. 1–27. https://doi.org/10.1007/s00348-016-2157-1

[18] Bosbach, J., Schanz, D., Godbersen, P., and Schroeder, A., "Dense Lagrangian Particle Tracking of Turbulent Rayleigh Benard Convection in a Cylindrical Sample Using Shake-The-Box," *17th European Turbulence Conference (ETC)*, 2019.

[19] Schanz, D., Novara, M., Geisler, R., Agocs, J., Eich, F., Bross, M., Kaehler, C. J., and Schroeder, A., "Large-Scale Volumetric Characterization of a Turbulent Boundary Layer Flow," *13th International Symposium on Particle Image Velocimetry*, 2019.

[20] Jux, C., Sciacchitano, A., Schneiders, J. F. G., and Scarano, F., "Robotic Volumetric PIV of a Full-Scale Cyclist," *Experiments in Fluids*, Vol. 59, April 2017, Paper 74. https://doi.org/10.1007/s00348-018-2524-1

[21] Schneiders, J. F. G., Scarano, F., Jux, C., and Sciacchitano, A., "Coaxial Volumetric Velocimetry," *Measurement Science and Technology* Vol. 29, No. 6, 2018, Paper 065201. https://doi.org/10.1088/1361-6501/aab07d

[22] Schroeder, A., Schanz, D., Bosbach, J., Novara, M., Geisler, R., Agocs, J., and Kohl, A., "Large-Scale Volumetric Flow Studies on Transport of Aerosol Particles Using a Breathing Human Model with and Without Face Protections," *Physics of Fluids*, Vol. 34, No. 3, 2022, Paper 035133. https://doi.org/10.1063/5.0086383

[23] Faleiros, D. E., Tuinstra, M., Sciacchitano, A., and Scarano, F., "Generation and Control of Helium-Filled Soap Bubbles for PIV," *Experiments in Fluids*, Vol. 60, March 2019, Paper 929. https://doi.org/10.1007/s00348-019-2687-4

[24] Gibeau, B., and Ghaemi, S., "A Modular, 3D-Printed Helium-Filled Soap Bubble Generator for Large-Scale Volumetric Flow Measurements," *Experiments in Fluids*, Vol. 59, Dec. 2018, Paper 178.

[25] Faleiros, D. E., "Soap Bubbles for Large-Scale PIV: Generation, Control and Tracing Accuracy," Ph.D. Dissertation, Aerospace Engineering Dept., Delft Univ. of Technology, Delft, The Netherlands, 2021.

[26] Sciacchitano, A., Giaquinta, D., Schneiders, J. F. G., Scarano, F., van Rooijen, B. D., and Funes, D. E., "Quantitative Flow Visualization of a Turboprop Aircraft by Robotic Volumetric Velocimetry," *18th International Symposium on Flow Visualization*, 2018.

[27] Barata, J. M. M., Bernando, N., Santos, P. J. C. T., and Silva, A. R. R., "Experimental Study of a Ground Vortex: The Effect of the Crossflow Velocity," *49th AIAA Aerospace Sciences Meeting*, AIAA Paper 2011-1052, 2011

[28] Nguyen, D. T., Maher, B., and Hassan, Y., "Effects of Nozzle Pressure Ratio and Nozzle-to-Plate Distance to Flow-Field Characteristics of an Under-Expanded Jet Impinging on a Flat Surface," *Aerospace*, Vol. 6, No. 1, 2019, Paper 4. https://doi.org/10.3390/aerospace6010004

[29] Saripalli, K. R., "Visualization Studies of Jet Impingement Flows at McDonnel Douglas Research Laboratories," *3rd International Symposium on Flow Visualization*, 1983.

[30] Barata, J. M. M., Durao, D. F. G., and Heitor, M. V., "Impingement of Single and Twin Turbulent Jets Through a Crossflow," *AIAA Journal*, Vol. 29, No. 4, 1991, pp. 595–602.

[31] Barata, J. M. M., Durao, D. F. G., Heitor, M. V., and McGuirk, J. J., "On the Analysis of an Impinging Jet on Ground Effects," *Experiments in Fluids*, Vol. 15, No. 2, 1992, pp. 117–129.

[32] Wieneke, B., "Volume Self-Calibration for 3D Particle Image Velocimetry," *Experiments in Fluids*, Vol. 45, No. 4, 2008, pp. 549–556. https://doi.org/10.1007/s00348-008-0521-5

[33] Novara, M., Schanz, D., and Schroeder, A., "Two-Pulse 3D Particle Tracking with Shake-The-Box," *Experiments in Fluids*, Vol. 64, 2023. https://doi.org/10.1007/s00348-023-03634-7

[34] *FlowMaster Shake-the-Box: Product Manual*, LaVision, Goettingen, Germany, Sept. 2020, pp. 79–103.

[35] Raffel, M., Kaehler, C. J., Willert, C. E., Werely, S. T., Scarano, F., and Kompenhans, J., *Particle Image Velocimetry*, 3rd ed., Springer-Verlag, Berlin, 2018, Chap. 19. https://doi.org/10.1088/0957-0233/24/2/024009

[36] Adrian, R. J., "Dynamic Ranges of Velocity and Spatial Resolution of Particle Image Velocimetry," *Measurement Science and Technology* Vol. 8, No. 12, 1997, Paper 1393.

[37] Aguera, N., Cafiero, G., Astarita, T., and Discetti, S., "Ensemble 3D LPT for High Resolution Turbulent Statistics," *Measurement Science and Technology*, Vol. 27, No. 12, 2016, Paper 124011. https://doi.org/10.1088/0957-0233/27/12/124011

P. Lavoie
Associate Editor